Birefringence-Induced Heterogeneous Vector Pulses in Ultrafast Fiber Lasers

Dong Mao[1,*] Qun Gao,[1] Jingyi Li,[1] Zhiwen He,[1] Yueqing Du,[1] Chao Zeng,[1] Zhipei Sun,[2] and
Jianlin Zhao[1]

[1]*Key Laboratory of Light Field Manipulation and Information Acquisition, Ministry of Industry and Information
Technology, Shaanxi Key Laboratory of Optical Information Technology, School of Physical Science and
Technology, Northwestern Polytechnical University, Xi'an 710129, China*
[2]*Department of Electronics and Nanoengineering and QTF Centre of Excellence, Aalto University, FI-02150
Aalto, Finland*

Single-mode fiber lasers are capable of supporting trapped vector solitons with two similar orthogonally polarized components, due to the delicate balance between fiber birefringence and chromatic dispersion. Here, we demonstrate that heterogeneous vector pulses (HVPs) universally exist in anomalous-dispersion and near-zero-dispersion regimes, from hybrid-structure fiber lasers composed of low- and high-birefringent fibers. The vector pulses include two distinct orthogonally polarized components, one of which is a robust pulse, while the other is a gradually attenuated wavepacket composed of terahertz- (THz) repetition-rate subpulses. Simulation and analytical results fully reproduce experimental observations and demonstrate that the robust pulse couples a fraction of its energy to the orthogonally polarized component per roundtrip at the high-birefringent fiber, forming the unique HVPs. Apart from the intriguing nonlinear dynamics, the HVP can work as a flexible workhorse for various applications, ranging from optical polarization multiplexing to THz synthesis and optical precision spectroscopy.

I. INTRODUCTION

Vector solitons, the stable localized nonlinear waves typically comprising two similar orthogonally polarized components, are demonstrated in low-birefringent single-mode fibers (SMFs) [1–6]. The evolution dynamics of vector solitons can be well described by coupled nonlinear Schrödinger equations that include the chromatic dispersion, fiber birefringence, self-phase modulation, cross-phase modulation, and coherent-energy-exchange effects [7,8]. In SMFs, the group-velocity-locked vector solitons (i.e., trapped vector soliton) are demonstrated experimentally and theoretically [1,2], while the polarization-rotated vector solitons [3,4] and the phase-locked vector solitons [5,6] are only predicted theoretically. Similar vector solitons are also demonstrated in mode-locked SMF lasers [9–11]. However, the detailed evolution dynamics of solitons in fiber lasers may be different from that in SMFs, e.g., pairs of peaks and dips appear on the soliton spectrum due to the coherent energy exchange between two orthogonally polarized components [12]. In the aforementioned results, the birefringence of fibers or fiber lasers is confined to a small amount to achieve soliton trapping, and two orthogonally polarized components usually possess similar spectral and temporal profiles [13,14].

On the other hand, high-repetition-rate pulses attract a great deal of research interest due to their important applications in optical communications [15], terahertz (THz) wave generation [16], and frequency combs [17]. Due to the limitation of cavity lengths, the pulses delivered from mode-locked fiber lasers usually have megahertz to gigahertz (GHz) repetition rates [18–20]. By incorporating a microresonator into a fiber laser, couples of longitudinal modes can be selected and then locked via the four-wave mixing effect, giving rise to a series of uniformly separated pulses with repetition rates up to hundreds of GHz [21]. The repetition rates of pulses depend on the radius of the microresonator, and researchers must overcome the coupling difficulty between the fiber and microcavity [22]. Assisted by periodic filters, such as Mach-Zehnder or Fabry-Perot interferometers, fiber lasers can emit multiwavelength continuous waves, and their interference leads to packets of THz-repetition-rate pulses [23]. Due to unlocked phases between longitudinal modes in each wavelength, such wavepackets possess a strong noise background that is undesirable for applications. Thus, the direct generation of high-repetition-rate pulses or coherent wavepackets remains an urgent issue to be solved in ultrafast optics.

In previous schemes of birefringence-managed lasers, the polarization-maintaining fiber (PMF) usually combines with a polarizer and forms a Lyot filter to control the

---

*maodong@nwpu.edu.cn

wavelength and bandwidth of scalar solitons [24]. Notably, the case becomes more complex without polarizers or polarization-sensitive components. Besides the chromatic dispersion and nonlinear effects, the fiber birefringence and polarization orientation of pulses should be particularly considered in hybrid-structure fiber lasers comprising SMFs and PMFs; this differs from vector solitons in SMF lasers or scalar solitons in all-PMF lasers.

Here, we report on a unique type of vector pulse based on the periodic coupling and temporal splitting of two orthogonally polarized modes in SMF-PMF lasers. Unlike a vector soliton with two similar components, our vector pulse, referred to as a heterogeneous vector pulse (HVP), includes two distinct orthogonally polarized components, one of which is a robust pulse, while the other is a gradually attenuated high-repetition-rate wavepacket. Numerical simulations and analytical solutions fully interpret the experimental observations, and confirm that HVPs can be achieved in both anomalous-dispersion and near-zero-dispersion regimes.

II. PRINCIPLE AND EXPERIMENT SETUP

Two SMF-PMF fiber lasers with similar configurations are constructed to study the pulse evolution and validate the generality of the scheme. One of the fiber lasers operates in the anomalous-dispersion regime (approximately -0.12 ps^2) with a cavity length of about 12.7 m, while the other operates in the near-zero-dispersion regime (approximately -0.04 ps^2) with a cavity length of about 13.7 m (see details in part 1 of the Supplemental Material [25]). The configuration of the fiber lasers is shown in Fig. 1(a), consisting of a ring cavity, a pump-laser diode, and an output coupler. A carbon-nanotube saturable absorber initiates and sustains passive mode locking while a polarization-insensitive isolator ensures the unidirectional circulation of pulses.

The output pulses are monitored by an optical spectrum analyzer (Yokogawa AQ6370), a frequency-resolved optical gating (Femto Easy, FS-600), a high-speed oscilloscope (Tekronix 71604C), an autocorrelator (APE Pulsecheck USB-150), and a radio-frequency analyzer (Agilent E4440A).

The PMF, together with the polarization controller, governs the coupling behavior of two orthogonally polarized components inside the fiber laser. As illustrated in Fig. 1(b), the pulse can be resolved as two orthogonally polarized components along the fast axis and slow axis of the SMF, denoted as u_x and u_y, respectively. As a matter of routine, u_f and u_s represent two orthogonally polarized components along the fast axis and slow axis of the PMF, respectively. The angle θ between u_x and u_f dominates the coupling behavior of two orthogonally polarized modes. For a small θ, a fraction of u_x couples to u_s, while the majority of u_x couples to u_f. Due to polarization-mode
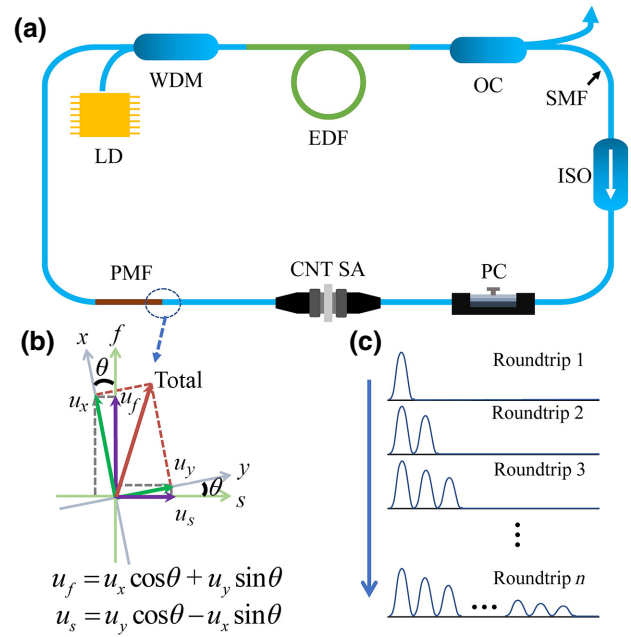

FIG. 1. Heterogeneous vector pulses in ultrafast fiber laser. (a) Sketch of the mode-locked fiber laser. WDM, wavelength-division multiplexer; EDF, erbium-doped fiber; OC, output coupler; ISO, polarization-insensitive isolator; PC, polarization controller; CNT SA, carbon-nanotube saturable absorber; PMF, polarization-maintaining fiber; LD, laser diode. (b) Coupling behavior of pulses from SMF to PMF. (c) Stronger component couples a small portion of energy to the weaker one per roundtrip, giving rise to a packet of gradually attenuated high-repetition-rate pulses.

coupling between the SMF and PMF, the stronger component in one polarization direction endows a small portion of its energy to the orthogonal polarization direction and forms a new weaker pulse per roundtrip. Consequently, the weaker component departs from the stronger one in the PMF and evolves to the high-repetition-rate wavepacket. Affected by the output coupler and saturable absorber, the subpulses gradually attenuate in the temporal domain, as sketched in Fig. 1(c).

III. EXPERIMENT RESULTS

In the anomalous-dispersion and near-zero-dispersion fiber lasers, self-starting mode-locking operations are established when the pump powers exceed about 16 and 15 mW, respectively, comparable with previous reports [26,27]. As elaborated in part 2 of the Supplemental Material [25], the pulses emitted from the anomalous-dispersion fiber laser exhibit soliton sidebands with locations following the relationship proposed by Kelly [28] and Taylor and co-workers [29]. Similarly, the pulses formed in the near-zero-dispersion regime display a smooth and broad spectrum, a typical characteristic of stretched pulses [30].

By slightly tuning the polarization orientation before the PMF with the polarization controller, both fiber lasers can directly emit stable HVPs. As shown in Figs. 2(a) and 2(b), pairs of birefringence-induced sidebands (BISs) appear on the output spectra of two lasers. Such BISs differ from previously reported Kelly sidebands (KSs) in anomalous-dispersion fiber lasers, as their intensities mainly depend on the polarization setting while locations rely on the PMF length, i.e., a similar sideband separation for two different fiber lasers with the same PMF length. The HVPs achieved in the near-zero-dispersion regime display pairs of BISs, which differ from traditional stretched pulses without any spectral sidebands [31]. Actually, similar sidebands are also observed in a dual-ring microresonator arising from the periodic coupling of cavity solitons [32]. By resolving the output pulse with a polarization beam splitter, we find that two orthogonally polarized components exhibit distinct properties: the u_x components are similar to the standard soliton or stretched pulse, while the u_y components display comblike profiles with a series of resonant peaks. Especially, the spectral peaks and dips appear in the same position, indicating a strong energy coupling between two components at these frequencies [33].

The temporal properties of HVPs are characterized by a frequency-resolved optical gating and further verified by an autocorrelator. As shown in Figs. 2(c) and 2(d), the temporal profiles of total pulses and their u_x components exhibit similar profiles for both fiber lasers. Interestingly, the u_y components are packets of gradually attenuated pulses, totally distinct from the u_x components. The repetition rates of subpulses in the wavepackets are about 750 and 774 GHz, respectively, which coincide with the

sideband separation of about 6.46 nm for the anomalous-dispersion fiber laser and about 6.31 nm for the near-zero-dispersion fiber laser. The retrieved pulses show periodic intensity modulations, indicating that the BISs are composed of phase-locked longitudinal modes rather than free-running incoherent continuous waves [34]. Akin to Kelly sidebands [35], the phase locking of these longitudinal modes is also realized by the saturable absorber, which is also similar to other frequencies of the pulse.

Although the profiles of the u_y components are somewhat like that of the Airy pulses [36], they have different physical properties and evolution behaviors. The durations of subpulses in the wavepacket are almost identical, while they decrease from peak to tail for Airy pulses. The HVP contains two distinct orthogonally polarized components, of which one is a robust pulse, while the other is a packet of gradually attenuated high-repetition-rate pulses, which fundamentally differ from the previously reported vector solitons in SMF lasers [37–39].

IV. SIMULATION RESULTS AND DISCUSSION

Based on the coupled Ginzburg-Landau equations, which incorporate birefringence, nonlinearity, dispersion, gain, and loss of a fiber resonator [40], we perform numerical simulations to unveil the formation and evolution behavior of HVPs. The simulation settings are the same as those of the experiments, and Eq. (1) is solved with the typical split Fourier method [8]:

$$
\frac{\partial u_x}{\partial z} = -i\beta u_x + \delta\frac{\partial u_x}{\partial t} - i\frac{k_2}{2}\frac{\partial^2 u_x}{\partial t^2} + i\gamma\left(|u_x|^2 + \frac{2}{3}|u_y|^2\right)u_x
$$
$$
+ \frac{i\gamma u_y^2 u_x^*}{3} + \frac{(g-l)}{2}u_x + \frac{g}{2\Omega_g^2}\frac{\partial^2 u_x}{\partial t^2},
$$

$$
\frac{\partial u_y}{\partial z} = i\beta u_y - \delta\frac{\partial u_y}{\partial t} - i\frac{k_2}{2}\frac{\partial^2 u_y}{\partial t^2} + i\gamma\left(|u_y|^2 + \frac{2}{3}|u_x|^2\right)u_y
$$
$$
+ \frac{i\gamma u_x^2 u_y^*}{3} + \frac{(g-l)}{2}u_y + \frac{g}{2\Omega_g^2}\frac{\partial^2 u_y}{\partial t^2}. \tag{1}
$$

Here, u_x and u_y represent the complex envelopes of two orthogonally polarized components along the fast and slow axes of the SMF, respectively. The propagation of the vector pulse in the PMF can also be described by Eq. (1). In this case, u_x and u_y also represent two orthogonally polarized components along the fast and slow axes of the PMF, respectively. t corresponds to the retardation time and z relates to the cavity position. Δn, $2\beta = 2\pi\Delta n/\lambda$, and $2\delta = 2\beta\lambda/2\pi c$ are the differences of refractive index, wave number, and inverse group velocity between the two components, respectively. k_2 is the second-order dispersion coefficient, l is the loss, and γ is the nonlinear coefficient. $g = g_0\exp(-E_p/E_s)$ is the saturable gain and Ω_g is the gain bandwidth, where E_p, g_0, and E_s relate to
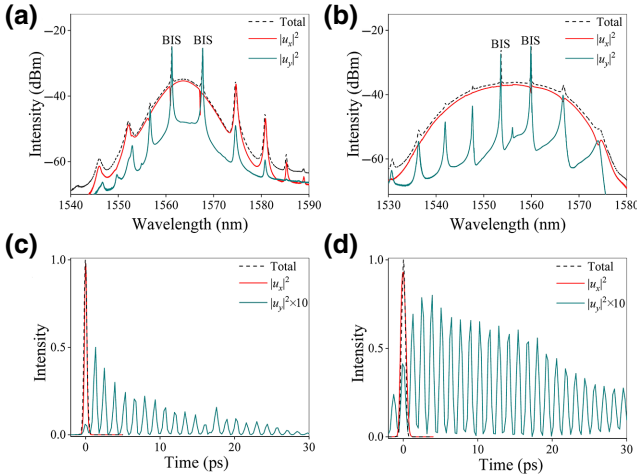
FIG. 2. Experimental results of HVPs in anomalous-dispersion and near-zero-dispersion fiber lasers. (a),(b) Spectra and (c),(d) retrieved profiles of the total pulses and their two orthogonally polarized components. HVPs and two components are amplified to perform frequency-resolved optical gating measurements.

the pulse energy, small-signal gain coefficient, and gain-saturation energy, respectively. The saturable absorber is modeled by $T = 0.49 - T_0/[1 + P_{(\tau)}/P_{sat}]$, where T_0 is the modulation depth, $P_{(\tau)}$ is the instantaneous power, and P_{sat} is the saturation power. For the anomalous-dispersion fiber laser, the simulation parameters are $\lambda = 1565$ nm, $\Omega_g = 40$ nm, $E_p = 40$ pJ, $g_0 = 3.14$ m^{-1}, $T_0 = 8\%$, and $P_{sat} = 15$ W. For the 3.6-m erbium-doped fiber (EDF) (Nufern, EDFL-980-HP), $\gamma = 3$ W^{-1} km^{-1}, $\Delta n = 0.9 \times 10^{-6}$, and $k_2 = 23.58$ ps^2 km^{-1}, while $\gamma = 1$ W^{-1} km^{-1}, $\Delta n = 0.9 \times 10^{-6}$, and $k_2 = -21.95$ ps^2 km^{-1} for the 8.1-m SMF. For the 1-m PMF, $\Delta n = 3.8 \times 10^{-4}$ and the other parameters are the same as those of the SMF. For the near-zero-dispersion fiber laser, the EDF (Nufern, EDFC-980-HP) length is 5.9 m, E_p is 85 pJ, g_0 is 0.7 m^{-1}, and β_2 is 22.51 ps^2 km^{-1}. The SMF has a length of 6.8 m, and the other parameters are the same as those of the anomalous-dispersion fiber laser.

The simulation starts from a low-intensity noise pulse. After one roundtrip, the output pulse is used as the initial signal for the next circulation. During propagation inside the cavity, each fiber component is considered by multiplying the corresponding matrix by the complex envelope of pulse. Especially, the coupling equation in Fig. 1(b) is incorporated into the model, and the operations of two fiber lasers depend on θ.

Figure 3 shows the simulation results for θ of 0, 0.03π, and 0.06π in two fiber lasers. The separations of adjacent BISs [lower panels of Figs. 3(a) and 3(c)] are 6.45 and 6.33 nm for two fiber lasers, which are comparable with those of the experimental results of 6.46 and 6.31 nm. Specifically, the pulse intensities and spectral peaks of the u_y components increase with θ, indicating that the mode-coupling effect dominates the formation of HVPs. For θ of 0.06π, the intensity of the u_x component is about 20 times higher than that of the u_y component. The sideband location and modulation period almost remain unchanged with θ for each fiber laser, which confirms that the coupling ratio does not affect the sideband separations. For θ further deviating from these values (0.1–0.4π), the fiber laser evolves to the other states. The simulation results quantitatively agree with the experimental observations, which confirm the validity of the simulation model.

Despite the intrinsic difference between the soliton pulse and stretched pulse, the formation and evolution dynamics of HVPs are quite similar for the anomalous-dispersion and near-zero-dispersion fiber lasers. For simplicity, the first case is discussed in detail in the following, while the latter is elaborated in part 4 of the Supplemental Material [25]. Figure 4 shows the simulated formation process of two orthogonally polarized components in the frequency and time domains, respectively. The u_x component gradually grows from a noise pulse to a robust soliton after about 50 roundtrips under the saturable-absorption, self-phase-modulation, and anomalous-dispersion effects
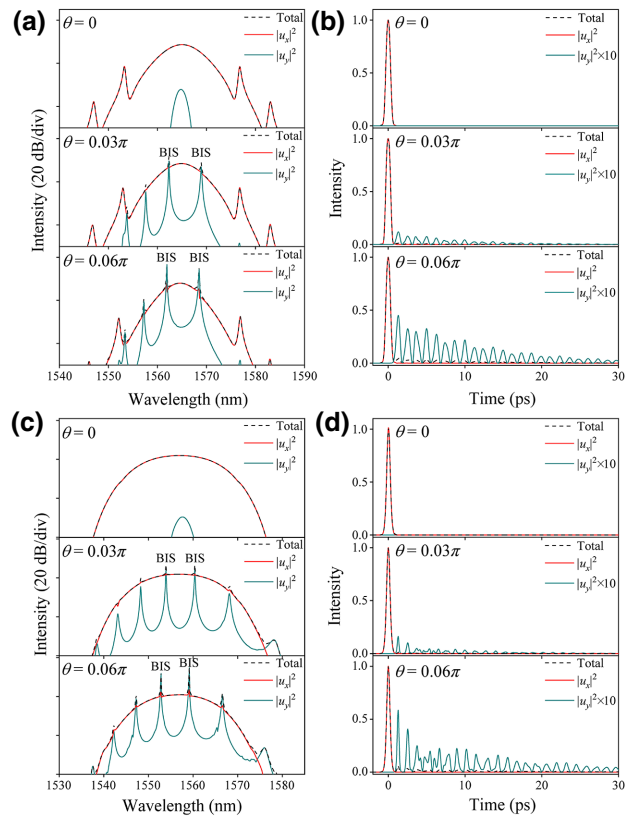

FIG. 3. Simulation results of HVPs in (a),(b) anomalous-dispersion and (c),(d) near-zero-dispersion fiber lasers. (a),(c) Spectra and (b),(d) temporal profiles of the total output pulses and their two orthogonally polarized components. θ is set as 0, 0.03π, and 0.06π from the top panel to the bottom panel for each fiber laser.

[Fig. 4(a) and 4(b)]; this is similar to the formation of standard solitons [41–43].

Interestingly, the u_y component displays distinct evolution behavior, in comparison with the u_x component or other vector solitons. As shown in Figs. 4(c) and 4(d), the BISs appear (approximately 30–150 roundtrips) and the initial pulse splits into two parts due to the birefringence-induced walk-off effect. With an increase in the roundtrips, the stronger pulse on the right side deviates from the u_x component and gradually vanishes after 150 roundtrips under the saturable-absorption and dispersion effects. The spectral and temporal evolutions show that the BISs correspond to a high-repetition-rate pulse, while the other parts relate to the deviated pulse. For a clear demonstration of the u_y component, only part of the time window is displayed in Fig. 4(d).

When the quasistable u_x component is formed (approximately 30 roundtrips), the weaker pulses appear on the u_y component and accompany the propagation of the u_x component [Figs. 4(b) and 4(d)]. The close-up evolution of this process is replotted in Figs. 4(e) and 4(f) to give a clear demonstration. One can observe that the new subpulses
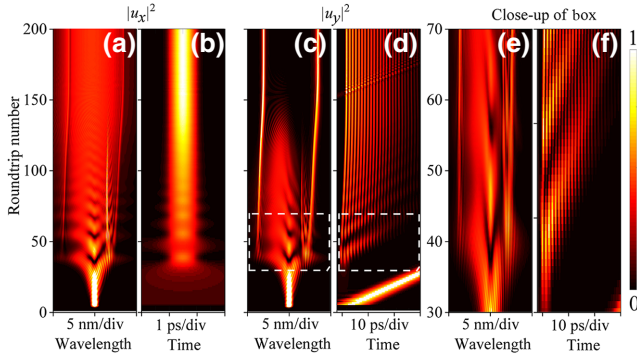
FIG. 4. Formation process versus roundtrips of HVPs in the anomalous-dispersion regime. (a) Spectrum and (b) pulse profile of the u_x component. (c) Spectrum and (d) pulse profile of the u_y component. (e),(f) Close-up of the box region in (c),(d), respectively. u_x and u_y components are normalized for a clear demonstration. As u_x and u_y components deviate from the time center with a ratio of about 0.6 ps per roundtrip, we plot the evolution process by subtracting the constant to study the evolution details within a limited time window.

are formed individually with an increase in roundtrip number. Simultaneously, two sharp spectra strive toward the resonant frequency with a stable separation that mainly depends on the birefringence of the PMF. Because the u_x and u_y components deviate from the center of the time window, with a ratio of about 0.6 ps per roundtrip, the locations of subpulses rely on the roundtrip number and appear at different time positions.

We further simulate the evolution dynamics of HVPs along the laser cavity. The u_x (u_f) intensity is about 20 times higher than the u_y (u_s) components, and both components are normalized for a clear demonstration, as shown in Fig. 5. The pulse first propagates through the 1-m SMF and is amplified by the 3.6-m EDF. Then, 30% of the
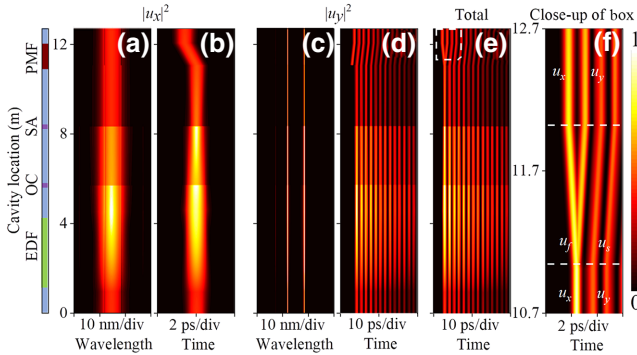
pulse energy is extracted by the coupler. After passing through the saturable absorber, the compressed pulse in the SMF reaches the PMF. At the connection point, most of the u_x component couples to the u_f component, while a fraction of the u_x component couples to u_s component, as shown in Figs. 5(e) and 5(f). The u_f component along the fast axis of the PMF dominates the propagation direction of the pulse. Governed by the fiber birefringence, the u_s component moves in the opposite direction and forms the subpulses deviating linearly from the u_f component. The two orthogonally polarized components depart from each other linearly from 1.22 to 2.58 ps in the PMF, while remaining unmoved in the rest of cavity, indicating that they are not trapped in the fiber laser. Such a physical process appears in each roundtrip and finally results in a packet of gradually attenuated high-repetition-rate pulses. It is worth noting that the u_x (u_f) component deviates from the time center per roundtrip due to the birefringence of the PMF, which is also validated by the building-up process shown in Fig. 4.

The formation mechanisms of HVPs and their BISs can be simply explained by a phase-matching principle that takes into account the fiber birefringence and nonlinear phase accumulated throughout the cavity [44]. The HVPs experience a PMF-induced energy redistribution in the resonator, and they emit new frequencies to realize self-consistent evolution. Due to the small coupling angle, the u_x component dominates the pulse evolution, while it disperses a fraction of its energy to the u_y component. Thus, new frequencies are released over the whole spectrum and propagate at different velocities with respect to the central frequency. Similar to the formation of KSs [28,29], only certain phase-locked frequencies satisfy the phase-matching condition that depends on the dispersion and nonlinearity of the cavity. As the influence of group-velocity dispersion is much smaller than the birefringence, it can be ignored in our analysis. A detailed derivation of the phase difference is given in part 5 of the Supplemental Material [25]. For each roundtrip, it can be expressed as

$$\Delta\varphi = a\Delta\omega - \phi_{\mathrm{NL}}, \quad a = \frac{1}{2c}\sum_i \Delta n_i L_i. \quad (2)$$

$\Delta\omega$ is the frequency offset between the central frequency of the u_x component and the sideband of the u_y components. $a\Delta\omega$ and ϕ_{NL} account for the phase difference induced by the fiber birefringence and nonlinear effects in a single roundtrip, respectively. Δn_i is the refractive-index difference between two orthogonally polarized components for a fiber with a length of L_i.

Such a newly emerging frequency in each period interferes destructively except at frequencies that are phase matched, i.e., $\Delta\varphi$ is the integer multiple of 2π. These frequencies will interfere constructively and form spectral sidebands when the frequency offset satisfies the

FIG. 5. Intracavity evolution of HVPs in the anomalous-dispersion regime. (a) Spectrum and (b) pulse profile of the u_x component. (c) Spectrum and (d) pulse profile of the u_y component. (e) Total pulse profile. (f) Close-up of the box region in (e). u_x and u_y components in (a)–(f) are normalized for a clear demonstration.
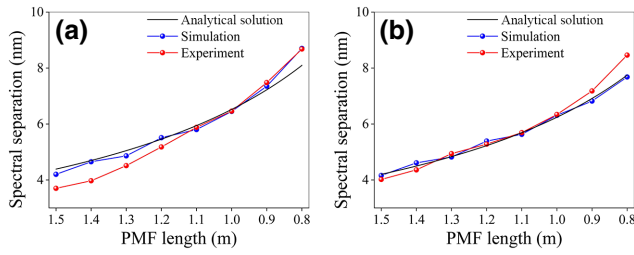
FIG. 6. Spectral separations of the u_y component versus PMF length in (a) anomalous-dispersion and (b) near-zero-dispersion fiber lasers.

phase-matching condition in Eq. (2), giving the angular frequency offset between the central frequency and sidebands:

$$\Delta\omega = \frac{\phi_{\mathrm{NL}} + 2m\pi}{a} \ .$$ (3)

Experimental results confirm that the separation of two BISs mainly depends on the length of the PMF. As shown in Figs. 6(a) and 6(b), by decreasing the PMF length from 1.5 to 0.8 m in the anomalous-dispersion (near-zero-dispersion) fiber laser, the spectral separation increases from 3.7 (4.02) to 8.68 m (8.46 m). The frequency difference changes from 0.45 (0.5) to 1.06 THz (1.05 THz). Such pulses can be applied for different-frequency THz-wave generation with a 4-dimethylamino-N-methyl-4-stilbazaliumtosylate crystal and may have a higher conversion efficiency than those of dual-wavelength continuous waves [45]. Based on the experimental parameters, we analytically calculate and simulate the evolution of sideband separation as a function of the PMF length using Eq. (3) for $m = -1$ and the Ginzburg-Landau equations, respectively. All of these results agree well with the experimental observations and confirm the accuracy of the analysis.

V. CONCLUSION

Based on the linear coupling of two polarization modes in SMF-PMF lasers, we demonstrate HVPs composed of two distinct orthogonally polarized components, of which one is a robust pulse, while the other is a gradually attenuated high-repetition-rate wavepacket. In each roundtrip, the stronger component endows a fraction of energy to the orthogonally polarized component at the connection point of the SMF and PMF. As two components have unequal group velocities, the periodic coupling and splitting, together with the cavity effect, lead to the unique HVPs. Simulation and experimental results validate that such HVPs can be universally obtained in both the anomalous-dispersion and near-zero-dispersion regimes. The formation of high-repetition-rate wavepackets mainly depends on the birefringence-related phase-matching effect, which

indicates a unique pulse-shaping mechanism under the periodic birefringence modulation. From the perspective of applications, such fiber lasers simultaneously produce two orthogonally polarized nonlinear waves with distinct properties, which can work as cost-effective multifunctional pulse sources. Especially, the high-repetition-rate wavepacket is quite attractive for applications of different-frequency THz-wave generation and field-enhancement Raman microscopy.

[1] C. R. Menyuk, Stability of solitons in birefringent optical fibers. I: Equal propagation amplitudes, Opt. Lett. **12,** 614 (1987).

[2] M. Islam, C. Poole, and J. Gordon, Soliton trapping in birefringent optical fibers, Opt. Lett. **14,** 1011 (1989).

[3] K. Blow, N. Doran, and D. Wood, Polarization instabilities for solitons in birefringent fibers, Opt. Lett. **12,** 202 (1987).

[4] V. Afanasjev, Soliton polarization rotation in fiber lasers, Opt. Lett. **20,** 270 (1995).

[5] D. N. Christodoulides and R. Joseph, Vector solitons in birefringent nonlinear dispersive media, Opt. Lett. **13,** 53 (1988).

[6] N. Akhmediev, A. Buryak, J. Soto-Crespo, and D. Andersen, Phase-locked stationary soliton states in birefringent nonlinear optical fibers, J. Opt. Soc. Am. B **12,** 434 (1995).

[7] S. G. Evangelides, L. F. Mollenauer, J. P. Gordon, and N. S. Bergano, Polarization multiplexing with solitons, J. Lightwave Technol. **10,** 28 (1992).

[8] G. P. Agrawal, *Nonlinear Fiber Optics* (Academic Press, New York, 2001).

[9] S. T. Cundiff, B. C. Collings, and W. H. Knox, Polarization locking in an isotropic, modelocked soliton Er/Yb fiber laser, Opt. Express **1,** 12 (1997).

[10] N. Akhmediev, J. Soto-Crespo, S. Cundiff, B. Collings, and W. Knox, Phase locking and periodic evolution of solitons in passively mode-locked fiber lasers with a semiconductor saturable absorber, Opt. Lett. **23,** 852 (1998).

[11] S. T. Cundiff, B. Collings, N. Akhmediev, J. M. Soto-Crespo, K. Bergman, and W. Knox, Observation of Polarization-Locked Vector Solitons in an Optical Fiber, Phys. Rev. Lett. **82,** 3988 (1999).

[12] D. Tang, H. Zhang, L. Zhao, and X. Wu, Observation of High-Order Polarization-Locked Vector Solitons in a Fiber Laser, Phys. Rev. Lett. **101,** 153904 (2008).

[13] H. Zhang, D. Tang, L. Zhao, X. Wu, and H. Y. Tam, Dissipative vector solitons in a dispersion-managed cavity fiber

laser with net positive cavity dispersion, Opt. Express **17,** 455 (2009).

[14] M. Liu, A. Luo, Z. Luo, and W. Xu, Dynamic trapping of a polarization rotation vector soliton in a fiber laser, Opt. Lett. **42,** 330 (2017).

[15] U. Keller, Recent developments in compact ultrafast lasers, Nature **424,** 831 (2003).

[16] Y. Minami, T. Kurihara, K. Yamaguchi, M. Nakajima, and T. Suemoto, High-power THz wave generation in plasma induced by polarization adjusted two-color laser pulses, Appl. Phys. Lett. **102,** 041105 (2013).

[17] E. S. Lamb, D. R. Carlson, D. D. Hickstein, J. R. Stone, S. A. Diddams, and S. B. Papp, Optical-Frequency Measurements with a Kerr Microcomb and Photonic-Chip Supercontinuum, Phys. Rev. Appl. **9,** 024030 (2018).

[18] D. Ma, Y. Cai, C. Zhou, W. Zong, L. Chen, and Z. Zhang, 37.4 fs pulse generation in an Er:fiber laser at a 225 MHz repetition rate, Opt. Lett. **35,** 2858 (2010).

[19] A. Martinez and Z. Sun, Nanotube and graphene saturable absorbers for fibre lasers, Nat. Photonics **7,** 842 (2013).

[20] H. Zhang, Y. Zheng, D. Mao, C. Zeng, Y. Du, and J. Zhao, Morphology-Controllable Ultrafast Fiber Lasers Based on Intracavity Manipulation of Transverse Modes, Phys. Rev. Appl. **16,** 034045 (2021).

[21] M. Peccianti, A. Pasquazi, Y. Park, B. E. Little, S. T. Chu, D. J. Moss, and R. Morandotti, Demonstration of a stable ultrafast laser based on a nonlinear microcavity, Nat. Commun. **3,** 765 (2012).

[22] L. Razzari, D. Duchesne, M. Ferrera, R. Morandotti, S. Chu, B. Little, and D. Moss, CMOS-compatible integrated optical hyper-parametric oscillator, Nat. Photonics **4,** 41 (2010).

[23] D. Mao, X. Liu, Z. Sun, H. Lu, D. Han, G. Wang, and F. Wang, Flexible high-repetition-rate ultrafast fiber laser, Sci. Rep. **3,** 3223 (2013).

[24] K. Özgören and F. Ö. İlday, All-fiber all-normal dispersion laser with a fiber-based Lyot filter, Opt. Lett. **35,** 1296 (2010).

[25] See the Supplemental Material at http://link.aps.org/supplemental/10.1103/PhysRevApplied.18.044044 for more detailed discussions, which includes Refs. [30,31]. Section 1 illustrates the configuration and parameters of anomalous-dispersion and near-zero-dispersion fiber lasers. Section 2 demonstrates the standard soliton and stretched pulse. Section 3 demonstrates the formation and evolution dynamics of HVPs in a near-zero-dispersion fiber laser. Section 4 derives the phase-matching principle of sideband separations.

[26] J. Peng and H. Zeng, Triple-State Dissipative Soliton Laser via Ultrafast Self-Parametric Amplification, Phys. Rev. Appl. **11,** 044068 (2019).

[27] D. Mao, X. Liu, and H. Lu, Observation of pulse trapping in a near-zero dispersion regime, Opt. Lett. **37,** 2619 (2012).

[28] S. Kelly, Characteristic sideband instability of periodically amplified average soliton, Electron. Lett. **28,** 806 (1992).

[29] D. Noske, N. Pandit, and J. Taylor, Source of spectral and temporal instability in soliton fiber lasers, Opt. Lett. **17,** 1515 (1992).

[30] K. Tamura, E. Ippen, H. Haus, and L. Nelson, 77-fs pulse generation from a stretched-pulse mode-locked all-fiber ring laser, Opt. Lett. **18,** 1080 (1993).

[31] S. K. Turitsyn, B. G. Bale, and M. P. Fedoruk, Dispersion-managed solitons in fibre systems and lasers, Phys. Rep. **521,** 135 (2012).

[32] A. Tikan, J. Riemensberger, K. Komagata, S. Hönl, M. Churaev, C. Skehan, H. Guo, R. N. Wang, J. Liu, P. Seidler, and T. J. Kippenberg, Emergent nonlinear phenomena in a driven dissipative photonic dimer, Nat. Phys. **17,** 604 (2021).

[33] H. Zhang, D. Tang, L. Zhao, and N. Xiang, Coherent energy exchange between components of a vector soliton in fiber lasers, Opt. Express **16,** 12618 (2008).

[34] J. Schröder, D. Alasia, T. Sylvestre, and S. Coen, Dynamics of an ultrahigh-repetition-rate passively mode-locked Raman fiber laser, J. Opt. Soc. Am. B **25,** 1178 (2008).

[35] Y. Wang, F. Leo, J. Fatome, M. Erkintalo, S. G. Murdoch, and S. Coen, Universal mechanism for the binding of temporal cavity solitons, Optica **4,** 855 (2017).

[36] D. Abdollahpour, S. Suntsov, D. G. Papazoglou, and S. Tzortzakis, Spatiotemporal Airy Light Bullets in the Linear and Nonlinear Regimes, Phys. Rev. Lett. **105,** 253901 (2010).

[37] B. C. Collings, S. T. Cundiff, N. Akhmediev, J. M. Soto-Crespo, K. Bergman, and W. Knox, Polarization-locked temporal vector solitons in a fiber laser: experiment, J. Opt. Soc. Am. B **17,** 354 (2000).

[38] S. V. Sergeyev, C. Mou, A. Rozhin, and S. K. Turitsyn, Vector solitons with locked and precessing states of polarization, Opt. Express **20,** 27434 (2012).

[39] Z. Luo, Q. Ning, H. Mo, H. Cui, J. Liu, L. Wu, A. Luo, and W. Xu, Vector dissipative soliton resonance in a fiber laser, Opt. Express **21,** 10199 (2013).

[40] D. Tang, L.-M. Zhao, B. Zhao, and A. Liu, Mechanism of multisoliton formation and soliton energy quantization in passively mode-locked fiber lasers, Phys. Rev. A **72,** 043816 (2005).

[41] D. Mao, X. Liu, D. Han, and H. Lu, Compact all-fiber laser delivering conventional and dissipative solitons, Opt. Lett. **38,** 3190 (2013).

[42] G. Herink, B. Jalali, C. Ropers, and D. R. Solli, Resolving the build-up of femtosecond mode-locking with single-shot spectroscopy at 90 MHz frame rate, Nat. Photonics **10,** 321 (2016).

[43] J. Peng, M. Sorokina, S. Sugavanam, N. Tarasov, D. V. Churkin, S. K. Turitsyn, and H. Zeng, Real-time observation of dissipative soliton formation in nonlinear polarization rotation mode-locked fibre lasers, Commun. Phys. **1,** 20 (2018).

[44] D. Mao, Z. He, Y. Zhang, Y. Du, C. Zeng, L. Yun, Z. Luo, T. Li, Z. Sun, and J. Zhao, Phase-matching-induced near-chirp-free solitons in normal-dispersion fiber lasers, Light: Sci. Appl. **11,** 25 (2022).

[45] M. Tang, H. Minamide, Y. Wang, T. Notake, S. Ohno, and H. Ito, Tunable terahertz-wave generation from DAST crystal pumped by a monolithic dual-wavelength fiber laser, Opt. Express **19,** 779 (2011).